

PixIE: Prompted Pixel-Space Low-Light Image Enhancement

Ruirui Lin Guoxi Huang David Bull Nantheera Anantrasirichai*
 Visual Information Laboratory, University of Bristol, United Kingdom

Abstract

Low-light images suffer from severe noise, contrast loss, and semantic ambiguity, making enhancement a joint problem of denoising and detail recovery. We propose PixIE, a feed-forward pixel-space LLIE framework semantically prompted by a vision foundation model. PixIE first performs cross-scale denoising to suppress noise and preserve structure, then refines details using DINO-Prompted Pixel Blocks (DPPBs), which inject intermediate DINOv3 features through patch-conditioned, spatially continuous per-pixel modulation. To make pixel-space attention efficient across scales, we introduce Spatial-Channel Compaction (SCC), which jointly reduces the spatial token grid and channel dimension. We further propose Multi-Receptive-Field Pixel Embedding (MRPE) to provide neighborhood-aware pixel representations before semantic prompting, improving robustness to signal-dependent noise beyond point-wise embeddings. Experiments on LLIE benchmarks show that PixIE improves average PSNR by 1.9–15.0% over recent state-of-the-art methods and reduces LPIPS by 8.5–44.4%. Qualitative comparisons further show sharper details and more stable textures, improving both reconstruction fidelity and perceptual quality.

1. Introduction

Low-light image enhancement (LLIE) is more than brightness adjustment. Real low-light images suffer from severe signal-dependent noise, texture collapse, and color distortion, making enhancement a coupled problem of denoising, contrast restoration, and semantically consistent detail recovery. LLIE is also important for downstream vision tasks such as detection, tracking, and recognition in autonomous driving, surveillance, and robotics, where poor illumination can substantially degrade algorithm performance.

Recent deep LLIE methods based on Convolutional Neural Networks [29], Transformers [48, 50], Mamba models [58], diffusion models [13], and Retinex-inspired hybrids [1, 2] have achieved significant progress. However,

*This work was supported by UKRI MyWorld Strength in Places Programme (SIPF00006/1).



Figure 1. Visual comparison of RetinexFormer [2], CIDNet [50], and PixIE (Ours) on an example LoLv2-Real test image. The low-light input is histogram-stretched to match the ground truth for better noise visualization. PixIE demonstrates superior noise suppression and detail restoration.

data-driven models are limited by their training data, making it difficult to capture priors beyond the training distribution. In severely underexposed regions, noise and texture become difficult to distinguish, often leading to over-smoothing, color drift, or inconsistent enhancement across semantic regions [47]. This motivates the use of external semantic priors learned beyond standard LLIE datasets.

Several restoration methods have explored foundation-model features from CLIP [38], Segment Anything Model (SAM) [39], and DINO [35, 41] as guidance signals [20, 30, 37]. Our analysis shows that DINOv3 [41] provides robust dense features under low-light degradation, helping resolve semantic ambiguity in noisy regions with challenging illumination conditions, as shown in Fig. 2. Existing methods, however, usually inject such features through global, coarse, or patch-wise conditioning [28, 47], limiting their alignment with the pixel-level operations required for high-fidelity detail recovery. This can cause cross-region inconsistencies and over-smoothed local structures, but such effects are often overlooked because LLIE often prioritizes global illumination correction.

Several restoration methods have explored foundation-model features from CLIP [38], Segment Anything Model (SAM) [39], and DINO [35, 41] as guidance signals [20, 30, 37]. Our analysis shows that DINOv3 [41] provides robust dense features under low-light degradation, helping reduce semantic ambiguity in noisy regions, as shown in Fig. 2. Existing methods, however, usually inject such features through global, coarse, or patch-wise conditioning [28, 47], limiting their alignment with pixel-level opera-

tions for high-fidelity detail recovery. This can cause cross-region inconsistencies and over-smoothed local structures, effects often overlooked because LLIE tends to prioritize global illumination correction.

While pixel-space modeling better preserves high-frequency details, it also introduces two challenges. First, naive pixel-space attention is costly at high resolutions, making pixel-space enhancement underexplored [6, 12]. Second, many pixel-space architectures rely on point-wise (1×1) projections [52], which have no spatial receptive field. Under severe low-light noise, relying only on single-pixel statistics makes it difficult to separate structure from noise [7, 8, 46], motivating local context aggregation before semantic prompting.

In this paper, we propose **PixIE**, an end-to-end **Pixel-space LLIE** framework semantically prompted by a DINO encoder. To the best of our knowledge, PixIE is the first LLIE method to inject foundation-model semantics directly into a *pixel-space* restoration pipeline through spatially continuous, per-pixel AdaLN-Zero modulation. As shown in Fig. 1, PixIE suppresses severe low-light noise while preserving fine structures more effectively than recent LLIE methods. PixIE first applies a semantics-free cross-scale denoising stream to suppress severe noise while preserving coarse structure, then uses Multi-Receptive-Field Pixel Embedding (MRPE) to equip pixels with neighborhood context before semantic prompting. The resulting features are refined by DINO-Prompted Pixel Blocks (DPPBs), which use multi-depth DINO features to generate full-resolution, spatially continuous modulation fields instead of coarse global or patch-level conditioning. This enables semantically aware detail recovery without hard patch boundaries, which can be amplified under spatially varying illumination and exposure correction, as validated in Sec. 4.3. Finally, Spatial-Channel Compaction (SCC) makes pixel-space attention affordable across scales by jointly reducing the spatial token grid and channel dimension.

In summary, our main contributions are:

- We propose PixIE, a novel pixel-space LLIE framework that combines cross-scale denoising with DINO-guided semantic modulation for pixel-to-semantic enhancement.
- We introduce DPPB, which injects multi-depth DINO semantics through spatially continuous, per-pixel AdaLN-Zero modulation.
- We propose SCC to make pixel-space attention efficient by reducing both spatial tokens and channel dimensions.
- We introduce MRPE to aggregate multi-scale neighbourhood context before DPPB, improving robustness to signal-dependent noise.

2. Related Work

2.1. Low-light Image Enhancement (LLIE).

Traditional LLIE methods typically rely on hand-crafted priors and manual parameter tuning, and often suffer from over-amplification and halo artifacts. Representative approaches include histogram equalization [16] and Retinex-based methods [24], which decompose an image into illumination and reflectance components. Recent deep learning approaches have significantly advanced LLIE with end-to-end training and higher-capacity architectures. Representative directions include CNN-based methods [29, 31], Transformer-based methods [2, 48, 53], methods integrating Retinex-style decomposition into deep networks [1, 2, 45], conditional diffusion models that leverage generative priors [17, 18], and Mamba-based architectures for efficient global modeling [1, 14, 15, 58]. Several works [47, 57] further introduce semantic priors in feature space, while CID-Net [50] explores enhancement in an alternative color space (Horizontal/Vertical-Intensity) to better leverage chromaticity and intensity.

Despite these advances, many methods predominantly emphasize illumination correction and noise suppression, which can lead to over-smoothing and the loss of fine textures in practical and challenging low-light scenes. In contrast, PixIE injects foundation-model semantics through spatially continuous, pixel-wise modulation, enabling detail-preserving enhancement while remaining robust to heavy noise.

2.2. Pixel-Space Generative Models.

Latent-space pipelines [36, 40], commonly adopted in generative tasks, compress images into low-dimensional representations to improve computational efficiency. Meanwhile, their patch-based tokenization entangles the relationships between adjacent pixels, thereby weakening the fine-grained expressiveness of the output. This has become a bottleneck for latent-space generative models when pursuing high fidelity. To disentangle the strong correlations among pixels within a visual token, pixel-space modeling [12] has been proposed. By capturing dense per-pixel interactions, it ensures pixel independence and preserves high-frequency details. Recent trends in generative modeling have shifted toward pixel-space diffusion [5, 6, 33, 52, 56] to eliminate artifacts from lossy variational autoencoder [22] compression and patch-based tokenization. In the context of image enhancement, operating in pixel-space is crucial for texture fidelity, but it faces a similar trade-off: global attention mechanisms scale quadratically with the number of pixels [53], whereas standard 1×1 pixel-wise projections lack the receptive field to distinguish signal from noise [3].

Unlike generative models that prioritize global seman-

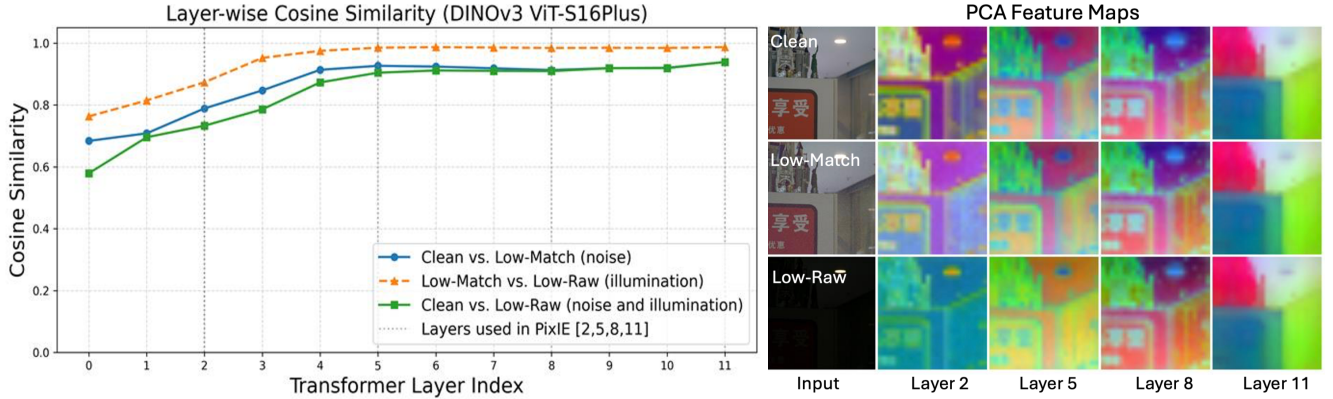


Figure 2. DINOv3 ViT-S/16 features under low-light degradation. **Left:** Mean token-wise cosine similarity across the 12 transformer layers for three comparisons: Clean vs. Low-Match (noise), Low-Match vs. Low-Raw (illumination), and Clean vs. Low-Raw (noise and illumination). Similarity increases with depth, indicating progressively more stable representations; dotted vertical lines mark the layers $\{2, 5, 8, 11\}$ used for PixIE conditioning. **Right:** PCA visualizations at selected layers show the same trend.

tic coherence through patch-based tokens [4, 52], PixIE adopts an end-to-end pixel-space framework tailored for image restoration. By avoiding strong pixel correlations and leveraging our proposed Spatial-Channel Compaction (SCC), it preserves the detail fidelity of pixel-space modeling while maintaining the computational efficiency required for high-resolution enhancement.

2.3. Foundation Models for Image Restoration.

Recent breakthroughs in Large-scale Foundation Models (FMs) such as CLIP [38], DINO [35, 41], and SAM [23, 39] have demonstrated remarkable robustness to image degradations. Consequently, several works have leveraged these semantic priors to guide image restoration tasks. For instance, CLIP features have been utilized to provide linguistic-visual descriptions that help stabilize color and style [30, 43, 49], while SAM has been employed to provide object-level masks for region-aware restoration tasks [26, 54]. However, integrating these semantic priors into a pixel-level restoration pipeline remains challenging and underexplored. Most existing methods inject FM features through global pooling or coarse patch-wise concatenation [28, 30, 54], which often leads to a semantic-spatial gap; the semantic information is too abstract to guide the recovery of fine-grained textures or to suppress pixel-level noise.

Our proposed DINO-Prompted Pixel Block (DPPB) departs from these coarse integration strategies by using DINOv3 features as a dynamic semantic pixel-level prompt. Unlike previous methods that treat FM features as static inputs, we utilize them to modulate a spatially continuous parameter field. This design allows the foundation model to provide high-level context while our pixel-space architecture performs the lifting of high-frequency detail recovery.

3. Methodology

As illustrated in Fig. 3, PixIE consists of three components: (i) *Cross-Scale Denoising*, which suppresses noise and preserves coarse structure using efficient Transformer blocks with fine-to-coarse feature propagation; (ii) *Pixel-Space Enhancement*, which enriches local context via Multi-Receptive-Field Pixel Embedding (MRPE) and enhances in pixel-space with injected semantics via DINO-Prompted Pixel Blocks (DPPB); and (iii) *Multi-Scale Fusion*, which aggregates the refined features from all scales to predict a residual enhancement.

Given a low-light input $I \in \mathbb{R}^{B \times 3 \times H \times W}$, we first extract features $F_0 \in \mathbb{R}^{B \times C \times H \times W}$ via a 3×3 convolution, expanding the channel capacity for subsequent transformer blocks. B is the batch size, (H, W) is the spatial resolution, and C is the channel dimension.

We then construct a three-scale pyramid $s \in \{1, 2, 3\}$, corresponding to resolutions of (H, W, C) , $(H/2, W/2, 2C)$, and $(H/4, W/4, 4C)$, respectively. The denoising stream operates fine-to-coarse and produces denoised features $\tilde{F}^{(s)}$. These are then processed by MRPE and a stack of N DPPBs (we set $N = 4$) to obtain semantically refined features $F^{(s)}$. Specifically, DINOv3 is frozen and executed once per input. We extract intermediate-layer tokens and resize the token grids to provide semantic prompts at all scales. Cross-scale propagation is restricted to the denoising stream (see Sec. 3.1): only denoised features $\tilde{F}^{(s)}$ are forwarded to the next coarser stage, while the refined DPPB outputs, $F^{(s)}$, are used only for final fusion and are not fed back into denoising blocks to avoid propagating semantically modulated pixel-space features across scales. Finally, we upsample $F^{(2)}$ and $F^{(3)}$ via PixelShuffle, concatenate them with $F^{(1)}$, and apply a simple Multi-Scale Fusion with two 3×3 convolutions to predict a residual R , yielding $\hat{I} = I + R$.

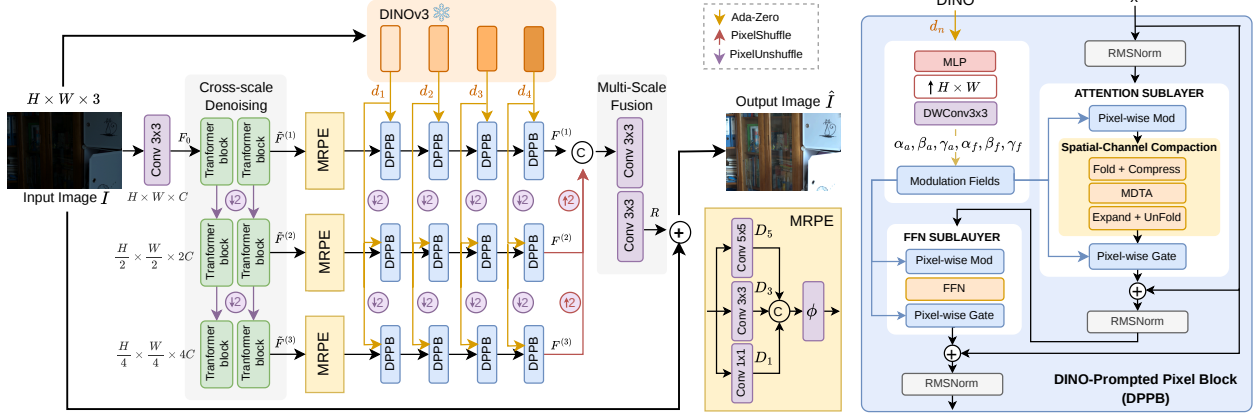


Figure 3. The overall pipeline of our proposed PixIE. Given a low-light input, the cross-scale denoising stream suppresses noise fine-to-coarse, followed by Multi-Receptive-Field Pixel Embedding (MRPE), and DINO-Prompted Pixel Blocks (DPPBs) inject DINO semantic guidance at each scale, and multi-scale fusion aggregates refined features to predict a residual correction $\hat{I} = I + R$.

3.1. Cross-Scale Denoising

The cross-scale denoising module produces a noise-suppressed, structurally preserved representation before semantic prompting. Under low-light conditions, severe noise and degradation corrupt local information, making alignment with high-level semantic priors unreliable and potentially unstable. To address this, we first apply the denoiser, keeping the denoising stream semantics-free and injecting DINO conditioning only after denoising (in DPPBs)—when semantic-to-pixel alignment becomes meaningful. Moreover, we propagate only denoised features across scales to avoid feeding semantically modulated activations back into the denoiser, which might introduce distribution shifts across scales.

We adopt a Transformer-based denoiser, as the self-attention mechanism can be viewed as a special case of non-local operations in the embedded Gaussian form [27]. For efficiency, we employ Restormer-style blocks, each composed of Multi-Dconv Head Transposed Attention (MDTA) followed by a Gated-Dconv Feed-Forward Network (GDFN). Since MDTA attends in the channel domain, its computational cost scales as $\mathcal{O}(HW \cdot C^2)$, *i.e.*, linearly with the number of pixels for a fixed channel width.

Rather than processing scales independently, we propagate features fine-to-coarse: each transformer block’s output is downsampled and fused into the corresponding block at the next coarser scale. This transfers fine-scale structure while enabling coarser branches to better suppress spatially correlated noise, without a dedicated encoder. At each scale s , the denoising stream contains two sequential transformer blocks $\mathcal{T}_1^{(s)}$ and $\mathcal{T}_2^{(s)}$. Let $\tilde{F}_0^{(s)}$ denote the input features at scale s . The blocks process features sequentially:

$$\tilde{F}_1^{(s)} = \mathcal{T}_1^{(s)}(\tilde{F}_0^{(s)}), \quad \tilde{F}_2^{(s)} = \mathcal{T}_2^{(s)}(\tilde{F}_1^{(s)}). \quad (1)$$

where $\tilde{F}^{(s)} = \tilde{F}_2^{(s)}$ denotes the denoised feature at scale s .

For scales $s > 1$, the output of each block at the finer scale is downsampled via PixelUnshuffle and fused with the corresponding block output at the current scale via concatenation:

$$\tilde{F}_k^{(s)} \leftarrow W_k^{(s)} \left([\tilde{F}_k^{(s)}; \text{Down}(\tilde{F}_k^{(s-1)})] \right), \quad (2)$$

$$k \in \{1, 2\}, \quad s \in \{2, 3\}.$$

where $[\cdot; \cdot]$ denotes channel-wise concatenation, $W_k^{(s)}$ is a learned channel projection, and $\text{Down}(\cdot)$ denotes PixelUnshuffle downsampling. The denoised features $\tilde{F}^{(s)}$ are then passed to MRPE and the DPPB stack at scale s .

3.2. Pixel-Space Enhancement

Multi-Receptive-Field Pixel Embedding (MRPE). We introduce Multi-Receptive-Field Pixel Embedding (MRPE) as a simple local context aggregation module placed before our pixel-level restoration blocks. MRPE computes three parallel embeddings with kernel sizes $k \in \{1, 3, 5\}$, capturing point-wise intensity information with local structural context. We allocate the embedding dimension C across the three branches to emphasize contextual cues: specifically, we assign 25% of the channels to the 1×1 branch and distribute the remaining 75% equally to the 3×3 and 5×5 branches, *i.e.*, $(D_1, D_3, D_5) = (0.25D, 0.375D, 0.375D)$. This design is motivated by characteristics of low-light degradations, where single-pixel intensities are often dominated by signal-dependent noise (whose variance scales with the pixel value); allocating fewer channels to the point-wise branch and more to larger receptive fields encourages neighborhood-aware representations for more robust denoising. The resulting features are concatenated and lin-

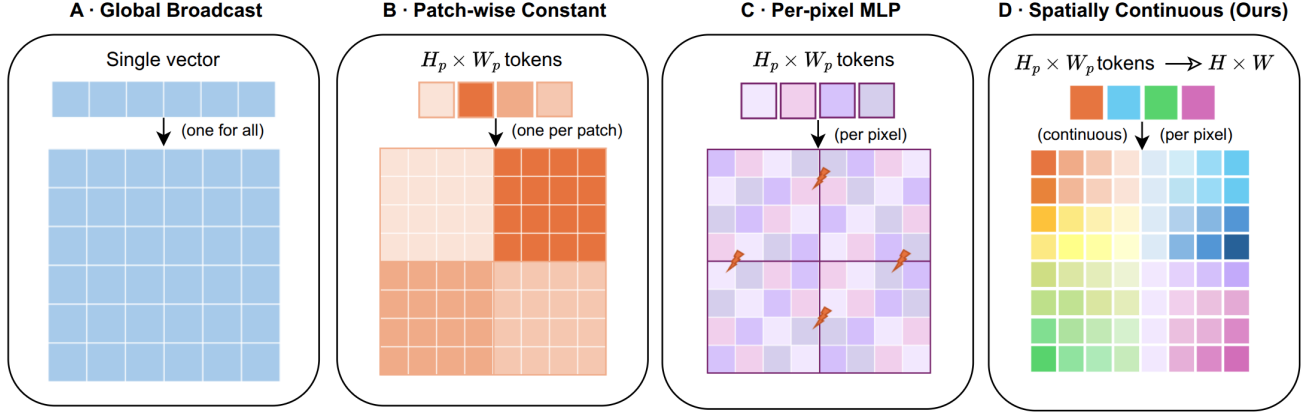


Figure 4. Patch-conditioned modulation strategy comparison: (A) Global broadcast applies one shared vector to all pixels. (B) Patch-wise constant uses one token per patch, yielding piecewise-constant modulation and grid seams at patch boundaries. (C) Per-pixel MLP predicts pixel-wise parameters within each patch, but independent per-patch prediction may introduce boundary discontinuities. (D) Ours upsamples the token grid to full resolution, producing a spatially continuous modulation field with no hard patch boundaries.

early mixed:

$$e = \phi\left(\left(f_1(\tilde{F}^{(s)}); f_3(\tilde{F}^{(s)}); f_5(\tilde{F}^{(s)})\right)\right),$$

where $(\cdot; \cdot)$ denotes channel-wise concatenation, $f_k(\cdot)$ denotes a $k \times k$ convolution and $\phi(\cdot)$ is a linear projection. By injecting multi-scale spatial context early, MRPE produces a denoising-friendly representation for our DINO-Prompted Pixel Blocks, mitigating point-source noise while retaining sharp edges and textures.

DINO-Prompted Pixel Block (DPPB). The proposed DPPB, shown in Fig. 3 (blue panel), is a pixel-level residual block that injects semantic guidance from a frozen foundation model (DINOv3) via *patch-conditioned, spatially continuous modulation*. Rather than using only the final-layer representation of the foundation model, which is highly invariant but may lose fine spatial details, we extract intermediate patch tokens from L selected layers of the frozen DINOv3 encoder. We set $L=4$ and take layers $\{2, 5, 8, 11\}$, denoting the resulting token grids as $\{d_n\}_{n=1}^L$. For each pyramid scale s , we resize all token grids to $H_p^{(s)} \times W_p^{(s)}$ and concatenate them to form the DPPB conditioning. The same concatenated tokens are used to prompt a stack of N DPPBs at each scale.

Given input features $d_x \in \mathbb{R}^{B \times C \times H \times W}$, we extract DINO tokens and reshape them into a 2D token grid $d_n \in \mathbb{R}^{B \times D_d \times H_p \times W_p}$, where $n \in \{1, \dots, L\}$, $H_p = H/P$ and $W_p = W/P$, with P denoting the patch size. A lightweight MLP predicts AdaLN-Zero parameters on this grid:

$$m_n = \text{MLP}(d_n) \in \mathbb{R}^{B \times 6C \times H_p \times W_p}. \quad (3)$$

In our prompted parameter modulation, we predict modulation on the token grid $m_n \in \mathbb{R}^{B \times 6C \times H_p \times W_p}$, and upsample it to a full-resolution, spatially smooth parameter field

$\hat{m}_n \in \mathbb{R}^{B \times 6C \times H \times W}$ via $\hat{m}_n = \text{DWConv}_{3 \times 3}(\text{Up}(m_n))$, where $\text{Up}(\cdot)$ upsamples via bilinear interpolation from $H_p \times W_p$ to $H \times W$, and DWConv denotes depth-wise convolution. This yields spatially smooth modulation and blends adjacent tokens near patch boundaries as shown in Fig. 4 D. This means our DPPB differs from PixelDiT [52] (see Fig. 4 C), which predicts P^2 pixel-wise parameter sets per token independently within each patch at $\mathcal{O}(D_d \cdot P^2 C)$ MLP cost, resulting in per-pixel but patch-discontinuous modulation with hard discontinuities at patch boundaries. Our approach predicts a single parameter set per token ($\mathcal{O}(D_d \cdot C)$ MLP cost), recovering pixel resolution via interpolation rather than prediction, achieving $P^2 \times$ fewer parameters in the conditioning MLP ($256 \times$ at $P=16$) while producing a smoother, continuous modulation field. In low-light enhancement, where spatially varying exposure corrections are large, patch-boundary discontinuities are particularly visible (see Fig. 7 in Sec. 4.3).

We split \hat{m}_n channel-wise into $\{\alpha_a, \beta_a, \gamma_a, \alpha_f, \beta_f, \gamma_f\}_n \in \mathbb{R}^{B \times C \times H \times W}$, corresponding to scale, shift, and gating for the attention (\cdot_a) and feed-forward (\cdot_f) sublayers. Let $\text{RMSNorm}(\cdot)$ denote Root Mean Square Normalization and $\text{Mod}(u; \alpha, \beta) = \alpha \odot u + \beta$. The attention (Att) and the feed-forward network (FFN) updates are

$$x \leftarrow x + \gamma_a \odot \text{Attn}(\text{Mod}(\text{RMSNorm}(x); \alpha_a, \beta_a)), \quad (4)$$

$$x \leftarrow x + \gamma_f \odot \text{FFN}(\text{Mod}(\text{RMSNorm}(x); \alpha_f, \beta_f)). \quad (5)$$

Spatial-Channel Compaction (SCC). To balance efficiency and visual quality, the SCC (yellow panel inside blue panel in Fig. 3) is applied only to the attention branch, while the FFN, responsible for per-pixel feature transformation, operates on the full-resolution feature map to preserve and restore local details.

Table 1. Quantitative comparison on LOLv1, LOLv2 (Real and Synthetic), and LSRW. Cells highlighted in red, orange, and yellow denote the best, second-best, and third-best results, respectively.

Methods	LOLv1			LOLv2-Real			LOLv2-Synthetic			LSRW		
	PSNR↑	SSIM↑	LPIPS↓	PSNR↑	SSIM↑	LPIPS↓	PSNR↑	SSIM↑	LPIPS↓	PSNR↑	SSIM↑	LPIPS↓
ZeroDCE [9]	14.86	0.562	0.372	18.06	0.580	0.352	17.71	0.815	0.169	15.87	0.443	0.411
EnlightenGAN [19]	17.48	0.652	0.322	18.64	0.677	0.309	16.57	0.734	0.220	17.11	0.463	0.406
RetinexFormer [2]	25.16	0.845	0.131	22.79	0.840	0.171	25.67	0.930	0.059	17.77	0.518	0.317
WaveMamba [58]	26.54	0.883	0.106	22.13	0.890	0.162	26.51	0.957	0.065	19.51	0.569	0.300
DiffLL [17]	26.34	0.845	0.217	28.86	0.876	0.207	28.65	0.940	0.082	19.28	0.552	0.350
CIDNet [50]	28.20	0.889	0.079	24.11	0.871	0.108	25.71	0.942	0.045	18.07	0.532	0.286
Restormer [53]	22.43	0.823	0.147	18.60	0.789	0.232	21.41	0.830	0.144	16.30	0.453	0.427
LLFlow [47]	25.13	0.872	0.117	26.20	0.888	0.137	24.81	0.919	0.067	16.26	0.457	0.390
PixIE (Ours)	27.07	0.876	0.073	29.08	0.902	0.089	29.10	0.950	0.042	19.87	0.532	0.271

Although MDTA avoids quadratic *spatial* attention, its *channel* attention scales as $\mathcal{O}(HW \cdot C^2)$, which becomes expensive in multi-scale design as C increases at coarser levels. To reduce this cost, we compact features in both spatial and channel dimensions before attention. Given $x \in \mathbb{R}^{B \times C \times H \times W}$, we first fold it into non-overlapping $P \times P$ patches, $x_{\text{fold}} \in \mathbb{R}^{B \times (CP^2) \times H_p \times W_p}$, where $H_p = H/P$ and $W_p = W/P$. We then apply a 1×1 projection to compress the inflated channels to an attention dimension $x_c \in \mathbb{R}^{B \times D_{\text{attn}} \times H_p \times W_p}$ (we use $D_{\text{attn}} = 16$), perform MDTA on x_c , and map back via a 1×1 expansion followed by patch unfolding. The resulting attention cost is $\mathcal{O}(H_p W_p \cdot D_{\text{attn}}^2)$, since MDTA is performed on the compact representation x_c . Compared to applying MDTA directly on x with cost $\mathcal{O}(HW \cdot C^2)$, spatial folding reduces the number of locations by a factor of P^2 ($HW \rightarrow H_p W_p$), while channel bottlenecking replaces the quadratic channel term C^2 with D_{attn}^2 (with $D_{\text{attn}} \ll CP^2$ in the folded space), making the attention cost insensitive to the increasing C at coarser scales.

4. Experiments

4.1. Experimental Settings

Datasets. We train and evaluate on LOLv1 [45] and LOLv2 [51], where LOLv2 contains real-captured and synthetic subsets. LOLv2-Real provides 789 paired images (predefined 689 for training, 100 for testing). We follow the standard train/test splits of 485/15 for LOLv1, 689/100 for LOLv2-Real, and 900/100 for LOLv2-Synthetic. We also include LSRW [11], a large-scale real-world paired dataset with 5650 image pairs captured across diverse scenes. For these paired datasets, we report full-reference distortion metrics PSNR and SSIM, along with the perceptual metric LPIPS [55]. For unpaired evaluation, we test on the unpaired LIME [10], NPE [44], MEF [32], DICM [25], and VV [42] datasets. As there is no ground truth, we use no-reference metrics: NIQE [34] and CLIP-IQA [43].

Implementation. Our model is implemented in PyTorch and trained with the Adam optimizer [21] for 1.2×10^5 iterations. The learning rate is initialized to 3×10^{-4} and cosine-annealed to 1×10^{-7} . During training, images are randomly cropped to 256×256 and augmented with random rotations and horizontal/vertical flips. To match the DINO-pretrained encoder, we use a 16×16 patch size. The training objective is $\mathcal{L} = \mathcal{L}_1 + \lambda \mathcal{L}_{\text{LPIPS}}$, where $\lambda = 0.1$, \mathcal{L}_1 denotes the ℓ_1 reconstruction loss, and $\mathcal{L}_{\text{LPIPS}}$ is the perceptual loss.

4.2. Performance Comparison

Quantitative results are shown in Tab. 1. PixIE achieves state-of-the-art performance in terms of PSNR and SSIM on three out of four datasets. Notably, although the challenging LSRW dataset is pixel-misaligned, PixIE achieves a PSNR of 19.87 dB, outperforming WaveMamba and DiffLL. On LOLv2-Real, PixIE surpasses DiffLL by 0.22 dB in PSNR and achieves a superior SSIM of 0.902. These results demonstrate that our pixel-space enhancement effectively balances noise suppression with structural fidelity, even in datasets like LSRW and LOLv2 that are captured under real, heavy low-light noise. Furthermore, PixIE achieves the best LPIPS scores on LOLv1 (0.073) and LOLv2-Real (0.089), indicating that our approach aligns better with human visual perception. On average across all datasets, our method achieves the highest PSNR (26.28 dB) and lowest LPIPS (0.119), while maintaining competitive SSIM. This demonstrates superior reconstruction fidelity and perceptual quality compared to existing methods.

We present qualitative results in Fig. 5. While WaveMamba suggests that high-frequency components have limited influence on LLIE, we observe that fine textures remain important in practice, especially under heavy low-light noise where they are easily suppressed by aggressive denoising or global illumination correction. In the top row (LOLv1), most methods fail to recover subtle clothing textures, whereas PixIE better preserves these high-frequency patterns. PixIE restores the fine details of the ping-pong ta-

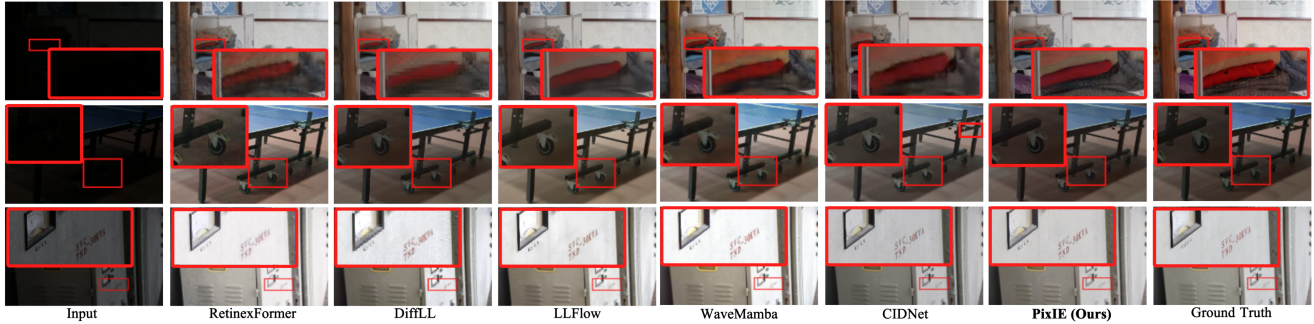


Figure 5. Qualitative comparison of PixIE with recent state-of-the-art methods on LOLv1, LOLv2-Real, and LSRW test sets.

Table 2. Quantitative comparison on five unpaired datasets: LIME, VV, DICM, NPE, and MEF. Cells highlighted in red, orange, and yellow denote the best, second-best, and third-best results, respectively.

Methods	LIME		VV		DICM		NPE		MEF	
	NIQE↓	CLIP-IQA↑	NIQE↓	CLIP-IQA↑	NIQE↓	CLIP-IQA↑	NIQE↓	CLIP-IQA↑	NIQE↓	CLIP-IQA↑
ZeroDCE [9]	3.76	0.454	2.96	0.350	4.00	0.513	3.95	0.458	3.29	0.514
EnlightenGAN [19]	3.92	0.390	3.01	0.290	3.53	0.457	4.01	0.364	3.48	0.483
RetinexFormer [2]	4.03	0.433	2.82	0.259	3.37	0.444	4.13	0.287	3.44	0.478
WaveMamba [58]	4.07	0.428	3.05	0.306	3.88	0.467	3.60	0.410	3.62	0.479
DiffLL [17]	3.78	0.254	3.51	0.264	3.85	0.211	4.31	0.206	3.66	0.200
CIDNet [50]	4.03	0.474	2.92	0.309	3.61	0.485	4.16	0.446	3.71	0.512
Restormer [53]	4.16	0.446	3.26	0.470	4.34	0.514	4.08	0.473	4.16	0.447
LLFlow [47]	5.26	0.296	5.48	0.296	5.53	0.304	6.92	0.297	6.43	0.265
PixIE (Ours)	4.23	0.478	2.78	0.333	3.77	0.541	3.93	0.450	3.40	0.515

ble wheels while maintaining effective noise suppression, as shown in the second row of Fig. 5. DiffLL, RetinexFormer, and WaveMamba attempt to handle the severe noise, but struggle to separate the table-leg boundary from the background floor, leading to residual artifacts or over-smoothing in large homogeneous regions. LLFlow further over-smooths the result, causing noticeable loss of texture and reduced color contrast. CIDNet also produces comparatively washed-out colors. In contrast, PixIE yields cleaner edges and more faithful textures and colors, consistent with its strong perceptual scores in Tab. 1 (e.g., LPIPS 0.089 on LOLv2-Real). Finally, on LSRW (third row), PixIE preserves high-frequency text details such as the red ‘SVC-30KVA’ lettering, where other methods exhibit color bleeding, character smoothing, or reduced local contrast. Overall, these results suggest that our pixel-space semantic modulation better separates structural high-frequency details from heavy noise, an area where standard LLIE methods often fail.

To further evaluate the generalization of PixIE, we conduct experiments on five widely used unpaired benchmarks: LIME, VV, DICM, NPE, and MEF. Quantitative results are shown in Tab. 2. Since these datasets lack Ground Truth images, we employ two no-reference image quality assessment metrics: NIQE, which measures naturalness (lower is better), and CLIP-IQA, which leverages a foundation model

Table 3. Ablation study of PixIE on LOLv2-Real dataset.

Variant	PSNR↑	SSIM↑	LPIPS↓
w/o Cross-scale Denoising	27.54	0.850	0.181
w/o MRPE	28.39	0.893	0.108
w/o DPPB	27.50	0.887	0.114
w DPPB w/o DINO	27.94	0.891	0.112
PixIE (Full)	29.08	0.902	0.089

to assess aesthetic and technical quality (higher is better). Across all datasets, our method consistently achieves top-three performance. Visual comparisons in Fig. 6 further illustrate the ability of our method to balance perceptual quality and distortion removal. In the coastal scene (bottom right), WaveMamba produces a clearer person but loses sky details, whereas our method preserves more scene information overall; the slightly darker subject can be easily corrected by post-processing without introducing noise or detail loss.

4.3. Ablation Study

We conduct ablations on LOLv2-Real dataset to evaluate the contribution of each component. We report quantitative results in Tab. 3 and Tab. 4, and provide visual comparisons in Fig. 7.

Tab. 3 demonstrates that removing Cross-scale Denois-

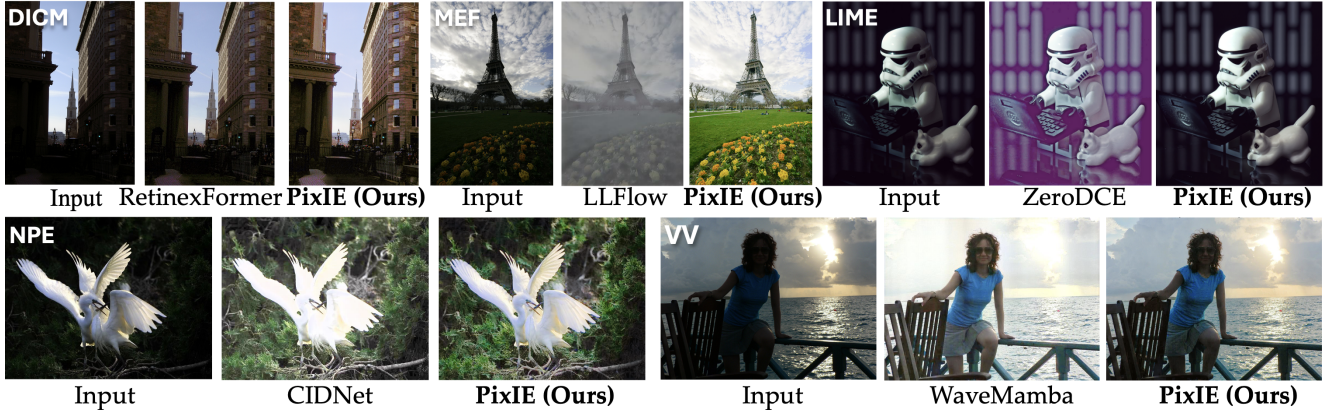


Figure 6. Qualitative comparison of PixIE with recent state-of-the-art methods on five unpaired datasets to show generalization.

Table 4. Ablation on attention dimension D_{attn} on LoLv2-Real. Complexity is measured on 256×256 inputs.

D_{attn}	PSNR \uparrow	SSIM \uparrow	LPIPS \downarrow	Params (M) \downarrow	GFLOPs \downarrow
16 (PixIE)	29.08	0.902	0.089	11.84	65.09
32	28.22	0.897	0.098	19.23	66.04
64	28.08	0.879	0.103	34.07	67.96

ing causes a large performance drop: PSNR decreases by 1.54 dB and LPIPS worsens from 0.089 to 0.181, confirming that suppressing severe low-light noise before semantic prompting is crucial for stable refinement. Replacing MRPE with a point-wise 1×1 embedding baseline (*i.e.*, no spatial context) reduces PSNR by 0.69 dB, indicating that local neighborhood aggregation is important for robust pixel-space enhancement under low-light noise. Finally, removing DPPB drops PSNR from 29.08 dB to 27.50 dB, while disabling DINO prompts within DPPB reduces PSNR to 27.94 dB (with correspondingly worse LPIPS), showing that the gain is driven by semantic prompting rather than the block structure alone.

As shown in Fig. 7, patchwise-constant modulation (panel i) produces visible grid seams from discontinuous exposure and color adjustments across patch boundaries. Replacing it with spatially continuous modulation (full mod), as shown in (panel ii), substantially reduces these seams while keeping attention disabled, confirming that modulation continuity is the primary cause of boundary artifact removal. The residual spatial inconsistency in panel (ii) reflects the absence of non-local feature interaction, which MDTA resolves to further recover fine texture and sharpness in full PixIE (panel iii).

Tab. 4 ablates the attention bottleneck D_{attn} . Increasing D_{attn} substantially raises model capacity with little or no accuracy gain, and can slightly reduce generalization. This supports our design choice of using a small bottleneck (e.g.,



Figure 7. Qualitative ablation results of PixIE on the LoLv2-Real dataset. ‘full mod’ denotes spatially continuous modulation in full resolution. We compare (i) w/o MDTA and w/o full mod, (ii) w/o MDTA and w full mod, and (iii) w MDTA and w full mod (full PixIE).

$D_{\text{attn}}=16$), which is sufficient for modeling pixel-space interactions while keeping the attention cost bounded.

5. Conclusion

We have introduced PixIE, a new feed-forward pixel-space framework for low-light image enhancement that integrates foundation-model semantics in pixel level through a spatially continuous modulation. PixIE separates the restoration process into a cross-scale denoising stream followed by DINO-guided pixel refinement, improving robustness under severe, signal-dependent noise. We also introduced the DINO-Prompted Pixel Block (DPPB), which converts DINOv3 patch tokens into a full-resolution, spatially smooth modulation field, enabling patch-conditioned yet pixel-wise semantic guidance without patch-boundary artifacts. To support efficient pixel-space modeling, we further proposed Multi-Receptive-Field Pixel Embedding (MRPE) for local context aggregation and Spatial-Channel Compaction (SCC) to reduce the cost of pixel attention in multi-scale. Experiments on standard LLIE benchmarks show that PixIE achieves strong quantitative (up to 15% PSNR improvement) and perceptually aligned performance while recovering fine textures in practical scenarios, enabling high-fidelity dense restoration.

References

- [1] Bai, J., Yin, Y., He, Q., Li, Y., Zhang, X.: Retinex-mamba: Retinex-based mamba for low-light image enhancement. In: International Conference on Neural Information Processing (2024) **1**, **2**
- [2] Cai, Y., Bian, H., Lin, J., Wang, H., Timofte, R., Zhang, Y.: Retinexformer: One-stage retinex-based transformer for low-light image enhancement. In: IEEE/CVF ICCV. pp. 12504–12513 (October 2023) **1**, **2**, **6**, **7**
- [3] Chang, M., Li, Q., Feng, H., Xu, Z.: Spatial-adaptive network for single image denoising. In: ECCV. pp. 171–187. Springer-Verlag, Berlin, Heidelberg (2020) **2**
- [4] Chen, S., Ge, C., Zhang, S., Sun, P., Luo, P.: PixelFlow: Pixel-space generative models with flow. arXiv preprint arXiv:2504.07963 (2025) **3**
- [5] Chen, Z., Zhu, J., Chen, X., Zhang, J., Hu, X., Zhao, H., Wang, C., Yang, J., Tai, Y.: Dip: Taming diffusion models in pixel space. arXiv preprint arXiv:2511.18822 (2025) **2**
- [6] Crowson, K., Baumann, S.A., Birch, A., Abraham, T.M., Kaplan, D.Z., Shippole, E.: Scalable high-resolution pixel-space image synthesis with hourglass diffusion transformers. In: ICML. JMLR.org (2024) **2**
- [7] Foi, A., Trimeche, M., Katkovnik, V., Egiazarian, K.: Practical poissonian-gaussian noise modeling and fitting for single-image raw-data. IEEE TIP **17**(10), 1737–1754 (2008) **2**
- [8] Gou, Y., Hu, P., Lv, J., Zhou, J.T., Peng, X.: Multi-scale adaptive network for single image denoising. In: NeurIPS. Curran Associates Inc. (2022) **2**
- [9] Guo, C.G., Li, C., Guo, J., Loy, C.C., Hou, J., Kwong, S., Cong, R.: Zero-reference deep curve estimation for low-light image enhancement. In: Proceedings of the IEEE conference on computer vision and pattern recognition (CVPR). pp. 1780–1789 (June 2020) **6**, **7**
- [10] Guo, X., Li, Y., Ling, H.: LIME: Low-light image enhancement via illumination map estimation. IEEE Trans. Image Process. **26**(2), 982–993 (2016) **6**
- [11] Hai, J., Xuan, Z., Yang, R., Hao, Y., Zou, F., Lin, F., Han, S.: R2rnet: Low-light image enhancement via real-low to real-normal network. Journal of Visual Communication and Image Representation **90**, 103712 (2023) **6**
- [12] Hoogeboom, E., Heek, J., Salimans, T.: Simple diffusion: end-to-end diffusion for high resolution images. In: ICML. ICML'23, JMLR.org (2023) **2**
- [13] Hou, J., Zhu, Z., Hou, J., Liu, H., Zeng, H., Yuan, H.: Global structure-aware diffusion process for low-light image enhancement. Advances in Neural Information Processing Systems **36**, 79734–79747 (2023) **1**
- [14] Huang, G., Lin, R., Li, Y., Bull, D., Anantrasirichai, N.: BVI-Mamba: video enhancement using a visual state-space model for low-light and underwater environments. In: Machine Learning from Challenging Data 2025. vol. 13460, pp. 74–81. SPIE (2025) **2**
- [15] Huang, G., Yang, Q., Qi, Z., Lin, R., Bull, D., Anantrasirichai, N.: Bayesian neural networks for one-to-many mapping in image enhancement. Proceedings of the AAAI Conference on Artificial Intelligence (2026) **2**
- [16] Ibrahim, H., Pik Kong, N.S.: Brightness Preserving Dynamic Histogram Equalization for Image Contrast Enhancement. IEEE Trans. Consumer Electronics **53**(4), 1752–1758 (2007) **2**
- [17] Jiang, H., Luo, A., Fan, H., Han, S., Liu, S.: Low-light image enhancement with wavelet-based diffusion models. ACM TOG **42**(6), 1–14 (2023) **2**, **6**, **7**
- [18] Jiang, H., Luo, A., Liu, X., Han, S., Liu, S.: Light-endiffusion: Unsupervised low-light image enhancement with latent-retinex diffusion models. In: ECCV (2024) **2**
- [19] Jiang, Y., Gong, X., Liu, D., Cheng, Y., Fang, C., Shen, X., Yang, J., Zhou, P., Wang, Z.: Enlightengan: Deep light enhancement without paired supervision. IEEE TIP **30**, 2340–2349 (2021) **6**, **7**
- [20] Jin, Z., Chen, S., Chen, Y., Xu, Z., Feng, H.: Let segment anything help image dehaze. arXiv preprint arXiv:2306.15870 (2023) **1**
- [21] Kingma, D.P., Ba, J.: Adam: A method for stochastic optimization. CoRR **abs/1412.6980** (2014) **6**
- [22] Kingma, D.P., Welling, M.: Auto-encoding variational bayes. In: ICLR (2014) **2**
- [23] Kirillov, A., Mintun, E., Ravi, N., Mao, H., Rolland, C., Gustafson, L., Xiao, T., Whitehead, S., Berg, A.C., Lo, W.Y., Dollár, P., Girshick, R.: Segment anything. arXiv:2304.02643 (2023) **3**
- [24] Land, E.H.: The retinex theory of color vision. Scientific American **237** **6**, 108–28 (1977) **2**
- [25] Lee, C., Lee, C., Kim, C.S.: Contrast enhancement based on layered difference representation of 2d histograms. IEEE Trans. Image Process. **22**(12), 5372–5384 (2013) **6**
- [26] Li, S., Liu, M., Zhang, Y., Chen, S., Li, H., Dou, Z., Chen, H.: SAM-deblur: Let segment anything boost image deblurring. In: ICASSP. pp. 2445–2449. IEEE (2024) **3**
- [27] Lin, J., Anantrasirichai, N., Bull, D.: Multi-scale denoising in the feature space for low-light instance segmentation. In: IEEE ICASSP. pp. 1–5 (2025) **4**
- [28] Lin, X., Yue, J., Chan, K.C., Qi, L., Ren, C., Pan, J., Yang, M.H.: Multi-task image restoration guided by robust DINO features. arXiv preprint arXiv:2312.01677 (2023) **1**, **3**

- [29] Lore, K.G., Akintayo, A., Sarkar, S.: LLNet: A deep autoencoder approach to natural low-light image enhancement. *Pattern Recognition* **61**, 650–662 (2017) [1](#), [2](#)
- [30] Luo, Z., Gustafsson, F.K., Zhao, Z., Sjolund, J., Schon, T.B.: Controlling vision-language models for multi-task image restoration. In: *ICLR* (2023) [1](#), [3](#)
- [31] Lv, F., Lu, F., Wu, J., Lim, C.: MBLLEN: Low-light image/video enhancement using cnns. In: *BMVC* (2018) [2](#)
- [32] Ma, K., Zeng, K., Wang, Z.: Perceptual quality assessment for multi-exposure image fusion. *IEEE Trans. Image Process.* **24**(11), 3345–3356 (2015) [6](#)
- [33] Ma, Z., Wei, L., Wang, S., Zhang, S., Tian, Q.: Deco: Frequency-decoupled pixel diffusion for end-to-end image generation. *arXiv preprint arXiv:2511.19365* (2025) [2](#)
- [34] Mittal, A., Soundararajan, R., Bovik, A.C.: Making a “completely blind” image quality analyzer. *IEEE Signal Process. Lett.* **20**(3), 209–212 (2013) [6](#)
- [35] Oquab, M., Darcet, T., Moutakanni, T., Vo, H.V., Szafraniec, M., Khalidov, V., Fernandez, P., Haziza, D., Massa, F., El-Nouby, A., Howes, R., Huang, P.Y., Xu, H., Sharma, V., Li, S.W., Galuba, W., Rabbat, M., Assran, M., Ballas, N., Synnaeve, G., Misra, I., Jegou, H., Mairal, J., Labatut, P., Joulin, A., Bojanowski, P.: DINOv2: Learning robust visual features without supervision (2023) [1](#), [3](#)
- [36] Peebles, W., Xie, S.: Scalable diffusion models with transformers. In: *IEEE/CVF ICCV*. pp. 4172–4182 (2023) [2](#)
- [37] Qi, C., Tu, Z., Ye, K., Delbracio, M., Milanfar, P., Chen, Q., Talebi, H.: Spire: Semantic prompt-driven image restoration. In: *ECCV*. pp. 446–464. Springer (2024) [1](#)
- [38] Radford, A., Kim, J.W., Hallacy, C., Ramesh, A., Goh, G., Agarwal, S., Sastry, G., Askell, A., Mishkin, P., Clark, J., Krueger, G., Sutskever, I.: Learning transferable visual models from natural language supervision. In: *ICML* (2021) [1](#), [3](#)
- [39] Ravi, N., Gabeur, V., Hu, Y.T., Hu, R., Ryali, C., Ma, T., Khedr, H., Rädle, R., Rolland, C., Gustafson, L., Mintun, E., Pan, J., Alwala, K.V., Carion, N., Wu, C.Y., Girshick, R., Dollár, P., Feichtenhofer, C.: SAM 2: Segment anything in images and videos. *arXiv preprint arXiv:2408.00714* (2024) [1](#), [3](#)
- [40] Rombach, R., Blattmann, A., Lorenz, D., Esser, P., Ommer, B.: High-resolution image synthesis with latent diffusion models. *CVPR* pp. 10674–10685 (2021) [2](#)
- [41] Siméoni, O., Vo, H.V., Seitzer, M., Baldassarre, F., Oquab, M., Jose, C., Khalidov, V., Szafraniec, M., Yi, S., Ramamonjisoa, M., Massa, F., Haziza, D., Wehrstedt, L., Wang, J., Darcet, T., Moutakanni, T., Sentana, L., Roberts, C., Vedaldi, A., Tolan, J., Brandt, J., Couprie, C., Mairal, J., Jégou, H., Labatut, P., Bojanowski, P.: DINOv3 (2025) [1](#), [3](#)
- [42] Vonikakis, V., Kouskouridas, R., Gasteratos, A.: On the evaluation of illumination compensation algorithms. *Multimedia Tools and Applications* **77**, 9211–9231 (2018) [6](#)
- [43] Wang, J., Chan, K.C., Loy, C.C.: Exploring CLIP for assessing the look and feel of images. In: *AAAI* (2023) [3](#), [6](#)
- [44] Wang, S., Zheng, J., Hu, H.M., Li, B.: Naturalness preserved enhancement algorithm for non-uniform illumination images. *IEEE Trans. Image Process.* **22**(9), 3538–3548 (2013) [6](#)
- [45] Wei, C., Wang, W., Yang, W., Liu, J.: Deep retinex decomposition for low-light enhancement. In: *BMVC* (2018) [2](#), [6](#)
- [46] Wei, K., Fu, Y., Zheng, Y., Yang, J.: Physics-based noise modeling for extreme low-light photography. *IEEE Trans. Pattern Anal. Mach. Intell.* **44**(11), 8520–8537 (2021) [2](#)
- [47] Wu, Y., Pan, C., Wang, G., Yang, Y., Wei, J., Li, C., Shen, H.T.: Learning semantic-aware knowledge guidance for low-light image enhancement. In: *IEEE/CVF CVPR* (2023) [1](#), [2](#), [6](#), [7](#)
- [48] Xu, X., Wang, R., Fu, C.W., Jia, J.: SNR-aware low-light image enhancement. In: *CVPR* (2022) [1](#), [2](#)
- [49] Xue, M., He, J., Wang, W., Zhou, M.: Low-light image enhancement via CLIP-fourier guided wavelet diffusion. *ACM TOMM* **21**(11) (Nov 2025) [3](#)
- [50] Yan, Q., Feng, Y., Zhang, C., Pang, G., Shi, K., Wu, P., Dong, W., Sun, J., Zhang, Y.: HVI: A new color space for low-light image enhancement. In: *IEEE/CVF CVPR*. pp. 5678–5687 (2025) [1](#), [2](#), [6](#), [7](#)
- [51] Yang, W., Wang, W., Huang, H., Wang, S., Liu, J.: Sparse gradient regularized deep retinex network for robust low-light image enhancement. *IEEE Trans. Image Process.* **30**, 2072–2086 (2021) [6](#)
- [52] Yu, Y., Xiong, W., Nie, W., Sheng, Y., Liu, S., Luo, J.: PixelDiT: Pixel diffusion transformers for image generation (2025) [2](#), [3](#), [5](#)
- [53] Zamir, S.W., Arora, A., Khan, S., Hayat, M., Khan, F.S., Yang, M.H.: Restormer: Efficient transformer for high-resolution image restoration. In: *CVPR* (2022) [2](#), [6](#), [7](#)
- [54] Zhang, Q., Liu, X., Li, W., Chen, H., Liu, J., Hu, J., Xiong, Z., Yuan, C., Wang, Y.: Distilling semantic priors from SAM to efficient image restoration models. *IEEE/CVF CVPR* pp. 25409–25419 (2024) [3](#)
- [55] Zhang, R., Isola, P., Efros, A.A., Shechtman, E., Wang, O.: The unreasonable effectiveness of deep fea-

- tures as a perceptual metric. In: IEEE/CVF CVPR (2018) [6](#)
- [56] Zheng, B., Ma, N., Tong, S., Xie, S.: Diffusion transformers with representation autoencoders. arXiv preprint arXiv:2510.11690 (2025) [2](#)
- [57] Zheng, S., Gupta, G.: Semantic-guided zero-shot learning for low-light image/video enhancement. In: Proceedings of the IEEE/CVF Winter conference on applications of computer vision. pp. 581–590 (2022) [2](#)
- [58] Zou, W., Gao, H., Yang, W., Liu, T.: Wave-Mamba: Wavelet state space model for ultra-high-definition low-light image enhancement. In: ACM MM (2024) [1, 2, 6, 7](#)

Supplementary Material: PixIE: Prompted Pixel-Space Low-Light Image Enhancement

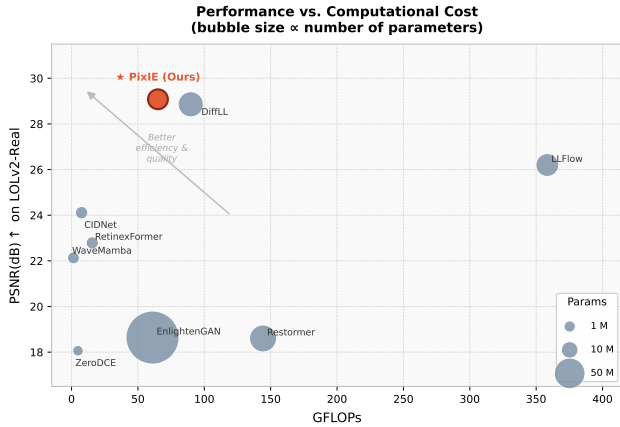


Figure 1. Performance vs. computational cost on LOLv2-Real in terms of PSNR. Higher PSNR indicates better fidelity. PixIE achieves the best trade-off.

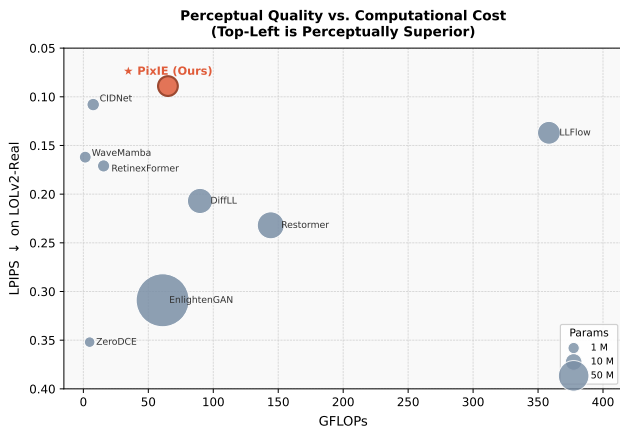


Figure 2. Performance vs. computational cost on LOLv2-Real in terms of LPIPS. Lower LPIPS indicates better perceptual quality; the y -axis is inverted for visual consistency. PixIE achieves the best trade-off.

A. Complexity Comparisons

We provide a detailed analysis of the computational complexity and performance trade-offs for PixIE compared to state-of-the-art low-light enhancement methods. Note that

Table 1. Model complexity and performance on LOLv2-Real.

Method	Params (M) \downarrow	GFLOPs \downarrow	PSNR \uparrow /SSIM \uparrow /LPIPS \downarrow
ZeroDCE [3]	0.075	4.83	18.06/0.580/0.352
EnlightenGAN [5]	114.35	61.01	18.64/0.677/0.309
RetinexFormer [1]	1.61	15.57	22.79/0.840/0.171
WaveMamba [10]	1.26	1.44	22.13/0.890/0.162
DiffLL [4]	22.08	89.79	28.86/0.876/0.207
CIDNet [8]	1.88	7.57	24.11/0.871/0.108
Restormer [9]	26.13	144.25	18.60/0.789/0.232
LLFlow [7]	17.43	358.4	26.20/0.888/0.137
PixIE (Ours)	11.84	65.09	29.08/0.902/0.089

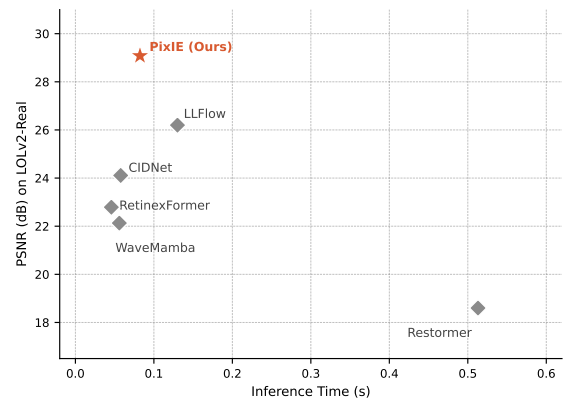


Figure 3. PSNR vs. inference time on LOLv2-Real (600×400 inputs). PixIE achieves the best quality among all supervised methods while maintaining competitive inference speed.

this analysis already includes the DINOv3 forward pass for reported GFLOPs and inference time. The reported 11.84 M parameters for PixIE are *trainable* parameters; frozen DINOv3 ViT-S/16 adds 21 M *non-trainable* parameters, giving 32.84 M total.

As illustrated in Fig. 1, Fig. 2, and Tab. 1, PixIE occupies the upper-left Pareto frontier across both fidelity (PSNR) and perceptual (LPIPS) metrics. Notably, while lightweight models such as CIDNet [8] and WaveMamba [10] offer lower GFLOPs, they exhibit a significant performance gap, with PixIE providing a substantial gain of over +5.0 dB in PSNR. Conversely, relative to the transformer-based Restormer [9], PixIE achieves a 10.48 dB PSNR improvement while using only 45.1% of the GFLOPs. It also outperforms the semantic-guided LLFlow [7], yield-

Method	Bic.	Boat	Bot.	Bus	Car	Cat	Chr.	Cup	Dog	Mot.	Ppl.	Tbl.	Mean
ZeroDCE	75.8	66.5	65.6	84.9	77.2	56.3	53.8	59.0	63.5	64.0	68.3	46.3	65.1
EnlightenGAN	79.6	73.0	71.4	85.6	80.4	60.5	64.1	69.4	72.7	63.2	77.5	43.2	70.1
Retinexformer	76.3	66.7	65.9	84.7	77.6	61.2	53.5	60.7	67.5	63.4	69.5	46.0	66.1
WaveMamba	81.9	78.2	70.5	86.5	80.6	64.9	67.2	73.6	77.5	66.4	79.1	41.8	72.3
DiffLL	81.6	71.4	67.7	83.9	77.1	57.7	62.4	64.4	70.3	60.6	73.1	44.2	67.8
CIDNet	82.8	75.4	71.8	84.7	80.1	59.9	64.5	69.2	75.7	64.3	78.4	41.0	70.7
Restormer	76.2	65.1	64.2	84.0	76.3	59.2	53.0	58.7	66.1	62.9	68.6	45.0	64.9
LLFlow+SFK	80.6	71.7	70.3	82.1	78.6	60.9	63.0	70.2	74.8	61.7	77.2	48.1	69.9
PixIE (Ours)	82.9	76.5	72.9	86.9	79.7	65.9	67.3	71.1	79.4	65.0	80.0	45.5	72.8

Table 2. Per-category object detection mean AP (%) on ExDark.

Table 3. Ablation on Spatial-Channel Compaction (SCC) design on LOLv2-Real dataset. C is the model dimension size. Complexity is measured on 256×256 inputs.

Variant	P	D_{attn}	PSNR \uparrow /SSIM \uparrow /LPIPS \downarrow	Params (M) \downarrow	GFLOPs \downarrow
No SCC	1	C	28.38/0.897/0.105	4.80	75.54
Channel only	1	16	27.82/0.896/0.102	4.30	66.24
Spatial only	16	$C \times P^2$	27.85/0.895/0.106	48.90	67.40
Full SCC (Ours)	16	16	29.08/0.902/0.089	11.84	65.09

ing higher PSNR (+2.88 dB) and lower LPIPS with $5.5 \times$ lower computational complexity, requiring only 18.2% of the GFLOPs. This demonstrates the high efficiency of our multi-scale design in balancing computational overhead with high-quality reconstruction.

For complexity evaluation, standard operators are profiled with fvcore. For Mamba-based architectures (e.g. WaveMamba [10]), FLOPs from custom CUDA ‘selective_scan’ modules are estimated analytically and added to the total because they are not fully supported by existing profilers. For fairness, diffusion-based models (e.g. DiffLL [4]) are evaluated using the FLOPs of their default inference pipeline with 10 sampling timesteps.

Fig. 3 reports inference time for supervised methods only to ensure a fair and directly comparable evaluation. Diffusion-based and unsupervised methods are excluded due to different inference procedures.

B. Downstream evaluation

Following the Retinexformer protocol, we evaluate object detection on ExDark, as shown in Tab. 2. PixIE achieves the best mean AP50, showing downstream benefit.

C. Spatial-Channel Compaction Analysis

The ablation results in Tab. 3 analyze our Spatial-Channel Compaction (SCC) design, demonstrating the trade-off between spatial sequence length and channel capacity in pixel-space attention. Using spatial-only compaction leads to a large parameter count (48.90M). Although spatial folding reduces the spatial grid by a factor of P^2 , it simultaneously increases the channel dimension to $C \times P^2$, which also enlarges the subsequent projection layers. In contrast,

channel-only compaction keeps a much smaller parameter count, but suffers from degraded performance and higher computational cost. Without SCC, the model has the highest computational cost (75.54 GFLOPs), and this cost scales further as the model dimension C grows. Our full SCC design combines spatial folding with channel compression to a fixed attention dimension $D_{\text{attn}}=16$, achieving the best performance. We attribute this improvement to joint compaction, which acts as a structured bottleneck and helps attention focus on more informative spatial-channel features. Although it introduces additional projection layers and parameters, compared to the channel-only variant, for channel compression and expansion, it still achieves the lowest GFLOPs by performing attention on a much smaller compacted token grid.

Patch Size. Note that we fix the patch size in Spatial-Channel Compaction to $P = 16$ by design. The spatial fold in SCC produces a compacted token grid of resolution $(H/P) \times (W/P)$, which must align with the DINOv3 ViT conditioning features in each DINO-Prompted Pixel Block (DPPB). Because DINOv3 uses a native patch size of 16×16 , setting $P = 16$ preserves this alignment without extra resampling. Changing P would likely break the correspondence between the token grid and the conditioning features, so an isolated ablation on P is difficult to interpret in the current architecture.

D. Effect of DINO Semantic Conditioning

Fig. 4 shows qualitative results with and without DINO semantic prompts. Without DINO features, the model exhibits a clear color shift. Adding DINO conditioning im-



Figure 4. Qualitative comparison with and without DINO semantic conditioning in the DINO-Prompted Pixel Block (DPPB). The left half shows results on LOL-v2 Real, and the right half shows results on LOL-v2 Synthetic. DINO conditioning improves color balance and brightness restoration, yielding results closer to the ground truth.

proves both color balance and scene brightness, producing results that more closely match the ground truth. This indicates that DINO semantic features provide a global semantic context that benefits both color and illumination restoration.

E. DINO Layer Selection

Tab. 4 studies the effect of DINO intermediate layer selection and shows that diverse features across depth are more effective than relying on any single stage. Using only the last layer ([11]) gives the weakest results, indicating that high-level semantics alone are not sufficient for low-light image reconstruction. Selecting only deep layers ([8, 9, 10, 11]) improves performance slightly, but remains suboptimal because these features lack fine low-level texture details. Early layers ([0, 1, 2, 3]) perform better, confirming the importance of shallow texture information, although the absence of stronger semantic information still limits reconstruction quality. In contrast, our uniformly distributed selection ([2, 5, 8, 11]) provides the most effective guidance by combining fine-grained textures with high-level semantics, and achieves the best overall performance.

Table 4. Ablation on DINO intermediate-layer selection (LOLv2-Real).

Layer selection	PSNR \uparrow	SSIM \uparrow	LPIPS \downarrow
[11]	27.38	0.894	0.100
[8, 9, 10, 11]	27.98	0.895	0.098
[0, 1, 2, 3]	28.40	0.899	0.105
[2, 5, 8, 11] (Ours)	29.08	0.902	0.089

F. Additional Ablation

Integration Approach Comparison. Results shown in the table Tab. 5 below demonstrate that, with fixed DINO features, continuous AdaLN-Zero performs best, confirming the benefit of our spatially continuous modulation.

MRPE Channel Allocation. Tab. 6 shows how channels are allocated across the three parallel branches of our pro-

Method	PSNR \uparrow	SSIM \uparrow	LPIPS \downarrow
Global broadcast	28.05	0.890	0.097
Patch-wise cond.	26.98	0.764	0.151
Cross-attn fusion	27.84	0.898	0.098
Ours (cont. AdaLN-Zero)	29.08	0.902	0.089

Table 5. Ablation of conditioning mechanisms on LOLv2-Real.

posed Multi-Receptive-Field Pixel Embedding (MRPE). An equal split (33/33/33) gives the weakest results. Replacing the multi-branch design with a single 3×3 convolution yields similar performance to the equal split, indicating that a naive larger receptive field, compared with the 1×1 point-wise embedding, is still insufficient to capture the range of context needed for low-light enhancement. Our allocation (25/37.5/37.5), which assigns fewer channels to the point-wise 1×1 branch and more to the 3×3 and 5×5 branches, achieves the best performance. This supports our design choice that, under low-light degradations, neighborhood-aware context is more important than point-wise intensity information alone.

Table 6. Ablation on MRPE channel allocation (LOLv2-Real).

Allocation	PSNR \uparrow	SSIM \uparrow	LPIPS \downarrow
Equal split (33/33/33)	27.51	0.892	0.111
Single Conv 3×3	27.58	0.894	0.107
Ours (25/37.5/37.5)	29.08	0.902	0.089

Modulation Field Upsampling. Tab. 7 compares strategies for upsampling the modulation field to the full resolution. PixelShuffle runs out of memory because it requires large full-resolution intermediate feature maps. Bicubic interpolation is more memory-efficient than PixelShuffle. Our design uses bilinear upsampling, which provides the best trade-off between restoration quality and efficiency. It avoids the memory overhead of learned upsampling while achieving the best results, with the lowest parameter count and competitive GFLOPs.

Table 7. Ablation on modulation field upsampling strategy. Metrics are reported on the LOLv2-Real dataset with complexity measured for 256×256 inputs.

Strategy	PSNR↑/SSIM↑/LPIPS↓	Params (M)↓	GFLOPs↓
PixelShuffle	OOM	123.32	813.33
Bicubic	28.22/0.897/0.103	19.23	65.34
Bilinear (PixIE)	29.08/0.902/0.089	11.84	65.09

G. UHD qualitative results

Below in Fig. 5, we show cropped UHD-LL [6] results against WaveMamba (UHD-based) and LLFlow+SFK (semantic-guided); PixIE denoises better while preserving details.

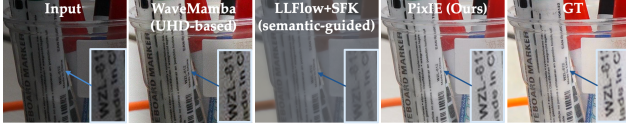


Figure 5. Qualitative results on UHD-LL dataset.

H. Failure Cases Analysis

We identify three limitations: (i) extreme non-uniform color casts from artificial lighting, where modulation may over-correct coherent regions; (ii) very small objects (< 16 px), which fall below the DINO patch resolution and receive weak semantic guidance; and (iii) compound degradations such as noise+blur+low-light [2], where PixIE is partially robust but not explicitly trained and will be considered as future work.

I. Transformer Block Details

In the Cross-Scale Denoising module, we use Restormer-style transformer blocks, each consisting of a Multi-Dconv Head Transposed Attention (MDTA) module followed by a Gated-Dconv Feed-Forward Network (GDFN). Details of each component are given below.

Multi-Dconv Head Transposed Attention (MDTA). Given an input feature map $X \in \mathbb{R}^{B \times D \times H \times W}$, we first apply normalization $Y = \text{Norm}(X)$ and form query, key, and value projections using a point-wise convolution followed by a depth-wise convolution:

$$Q = W_d^Q W_p^Q Y, \quad K = W_d^K W_p^K Y, \quad V = W_d^V W_p^V Y, \quad (1)$$

where $W_p^{(\cdot)}$ and $W_d^{(\cdot)}$ denote 1×1 point-wise and 3×3 depth-wise convolutions, respectively. MDTA then reshapes Q, K, V such that attention is computed in the *channel domain*, producing a transposed attention map of size

$D \times D$:

$$A = \text{Softmax}\left(\frac{\hat{K}\hat{Q}}{\alpha}\right), \quad (2)$$

$$\text{MDTA}(X) = W_o(\hat{V}A), \quad (3)$$

where $\hat{Q} \in \mathbb{R}^{HW \times D}$, $\hat{K} \in \mathbb{R}^{D \times HW}$, and $\hat{V} \in \mathbb{R}^{HW \times D}$ are reshaped tensors, α is a learnable scaling parameter, and W_o is a 1×1 output projection. We use a multi-head variant by splitting channels into h heads.

Gated-Dconv Feed-Forward Network (GDFN). Following MDTA, a gated feed-forward transformation is employed that combines channel mixing with local spatial aggregation:

$$U_i = W_d^i W_p^i \text{Norm}(X), \quad i \in \{1, 2\}, \quad (4)$$

$$\text{GDFN}(X) = W_p^0(\phi(U_1) \odot U_2). \quad (5)$$

where \odot denotes element-wise multiplication, $\phi(\cdot)$ is GELU, and $W_p^{(\cdot)}$ and $W_d^{(\cdot)}$ denote point-wise and depth-wise convolutions. Each Restormer block is applied in a residual form:

$$X \leftarrow X + \text{MDTA}(X), \quad X \leftarrow X + \text{GDFN}(X). \quad (6)$$

References

- [1] Cai, Y., Bian, H., Lin, J., Wang, H., Timofte, R., Zhang, Y.: Retinexformer: One-stage retinex-based transformer for low-light image enhancement. In: IEEE/CVF ICCV. pp. 12504–12513 (October 2023) 1
- [2] Feijoo, D., Benito, J.C., Garcia, A., Conde, M.V.: Darkir: Robust low-light image restoration. In: IEEE/CVF CVPR. pp. 10879–10889 (June 2025) 4
- [3] Guo, C.G., Li, C., Guo, J., Loy, C.C., Hou, J., Kwong, S., Cong, R.: Zero-reference deep curve estimation for low-light image enhancement. In: Proceedings of the IEEE conference on computer vision and pattern recognition (CVPR). pp. 1780–1789 (June 2020) 1
- [4] Jiang, H., Luo, A., Fan, H., Han, S., Liu, S.: Low-light image enhancement with wavelet-based diffusion models. ACM TOG **42**(6), 1–14 (2023) 1, 2
- [5] Jiang, Y., Gong, X., Liu, D., Cheng, Y., Fang, C., Shen, X., Yang, J., Zhou, P., Wang, Z.: Enlightengan: Deep light enhancement without paired supervision. IEEE TIP **30**, 2340–2349 (2021) 1
- [6] Li, C., Guo, C.L., Zhou, M., Liang, Z., Zhou, S., Feng, R., Loy, C.C.: Embeddingfourier for ultra-high-definition low-light image enhancement. In: ICLR (2023) 4

- [7] Wu, Y., Pan, C., Wang, G., Yang, Y., Wei, J., Li, C., Shen, H.T.: Learning semantic-aware knowledge guidance for low-light image enhancement. In: IEEE/CVF CVPR (2023) 1
- [8] Yan, Q., Feng, Y., Zhang, C., Pang, G., Shi, K., Wu, P., Dong, W., Sun, J., Zhang, Y.: HVI: A new color space for low-light image enhancement. In: IEEE/CVF CVPR. pp. 5678–5687 (2025) 1
- [9] Zamir, S.W., Arora, A., Khan, S., Hayat, M., Khan, F.S., Yang, M.H.: Restormer: Efficient transformer for high-resolution image restoration. In: CVPR (2022) 1
- [10] Zou, W., Gao, H., Yang, W., Liu, T.: Wave-Mamba: Wavelet state space model for ultra-high-definition low-light image enhancement. In: ACM MM (2024) 1, 2